Accuracy of Rotational and Divergent Kinetic Energy Spectra Diagnosed from Flight-Track Winds

LOTTE BIERDEL

Meteorologisches Institut, Ludwig-Maximilians-Universität, Munich, Germany

CHRIS SNYDER, SANG-HUN PARK, AND WILLIAM C. SKAMAROCK

National Center for Atmospheric Research,[a] Boulder, Colorado

(Manuscript received 26 January 2016, in final form 9 May 2016)

ABSTRACT

Under assumptions of horizontal homogeneity and isotropy, one may derive relations between rotational or divergent kinetic energy spectra and velocities along one-dimensional tracks, such as might be measured by aircraft. Two recent studies, differing in details of their implementation, have applied these relations to the Measurement of Ozone and Water Vapor by Airbus In-Service Aircraft (MOZAIC) dataset and reached different conclusions with regard to the mesoscale ratio of divergent to rotational kinetic energy. In this study the accuracy of the method is assessed using global atmospheric simulations performed with the Model for Prediction Across Scales, where the exact decomposition of the horizontal winds into divergent and rotational components may be easily computed. For data from the global simulations, the two approaches yield similar and very accurate results. Errors are largest for the divergent component on synoptic scales, which is shown to be related to a very dominant rotational mode. The errors are, in particular, sufficiently small so that the mesoscale ratio of divergent to rotational kinetic energy can be derived correctly. The proposed technique thus provides a strong observational check of model results with existing large commercial aircraft datasets. The results do, however, show a significant dependence on the height and latitude ranges considered, and the disparate conclusions drawn from previous applications to MOZAIC data may result from the use of different subsets of the data.

1. Introduction

The basic character of the atmospheric kinetic energy spectrum, with distinct power-law regimes at the synoptic scale (wavelengths on the order of a thousand kilometers) and the mesoscale (wavelengths from several hundred kilometers down to a few kilometers), separated by a transition on a scale of a few hundred kilometers, has long been established based on observational studies, especially those based on flight-track observations from aircraft (Nastrom et al. 1984; Nastrom and Gage 1985; Lindborg 1999). While there is a wide consensus about the crucial role of quasi-two-dimensional balanced motions in generating the shape of the kinetic energy spectrum on synoptic scales (Charney 1971), the dynamics underlying the mesoscale spectrum and its $-5/3$ power-law dependence on the horizontal wavenumber are a matter of ongoing debate (Gkioulekas and Tung 2006). It remains an open question whether the mesoscale spectrum follows mainly from inertia–gravity waves (VanZandt 1982; Dewan 1997) or from other types of motions, such as approximately two-dimensional vortical flow (Gage 1979; Lilly 1983) or stratified turbulence (Lindborg 2006). To a first approximation, a flow dominated by gravity waves can be distinguished from the other possibilities by an examination of the extent to which the horizontal velocity is associated mainly with horizontal divergence rather than vertical vorticity. The relative contribution of divergent and rotational energy to total kinetic energy is thus a key to understanding the main dynamical agent underlying the mesoscale energy spectrum.

---

[a] The National Center for Atmospheric Research is sponsored by the National Science Foundation.

Corresponding author address: Lotte Bierdel, Meteorologisches Institut, Theresienstrasse 37, 80333 Munich, Germany.
E-mail: lotte.bierdel@lmu.de

DOI: 10.1175/JAS-D-16-0040.1

A variety of atmospheric models, including both general circulation models and models used for numerical weather prediction, exhibit a shallowing of the mesoscale energy spectrum that is in reasonable agreement with the observed energy spectrum, especially in the lower stratosphere (Koshyk and Hamilton 2001; Skamarock 2004; Hamilton et al. 2008; Bierdel et al. 2012; Blažica et al. 2013; Brune and Becker 2013; Burgess et al. 2013; Ricard et al. 2013; Skamarock et al. 2014, hereafter S14). Model-simulated energy spectra, however, can be sensitive to details of the model configuration, including vertical resolution or strength of dissipation (Skamarock 2004; Brune and Becker 2013), and comparison of the spectral energy budgets between different models has shown marked differences (Frehlich and Sharman 2008; Augier and Lindborg 2013). Moreover, various models differ widely in their predictions for the relative magnitudes of rotational and divergent velocities at the tropospheric mesoscale. Blažica et al. (2013) examine the numerical weather prediction model ALADIN and find an equipartition of mesoscale rotational and divergent energy in the free troposphere of the midlatitudes. These findings are supported by the evaluation of data from global circulation models (GCMs) in S14 and Koshyk and Hamilton (2001). Contrarily, Hamilton et al. (2008) and Koshyk et al. (1999) find in several (high resolution) GCM simulations that upper-tropospheric kinetic energy is dominated by the rotational component. Thus, observational estimates of the energy spectra for the rotational and divergent flow will also be useful in identifying which numerical models produce mesoscale shallowing of the kinetic energy for the correct dynamical reasons.

Many observational studies addressing different aspects of the mesoscale energy spectrum with respect to geographical region and vertical levels found signs of mesoscale spectra dominated by either quasi-two-dimensional motion (Gage and Nastrom 1985; Cho et al. 1999) or unbalanced gravity wave motions (Vincent and Eckermann 1990; Bacmeister et al. 1996; Cho et al. 1999). Commercial aircraft observations, such as the Measurement of Ozone and Water Vapor by Airbus In-Service Aircraft (MOZAIC; Marenco et al. 1998) provide large global datasets of along- and across-track wind velocity measurements. Perhaps surprisingly, one-dimensional transects of horizontal wind components are useful for estimating the spectra of the divergent and rotational velocities. A method for doing this was first suggested by Lindborg (2007, hereafter L07), though basic results are also implicit in early work, such as Charney (1971). More recently, Bühler et al. (2014, hereafter B14) and Lindborg (2015, hereafter L15) have proposed approaches that are computationally simpler to implement than L07 and do not involve second-order differentiation of measurement data, which might introduce errors in the results. Both approaches have been applied to MOZAIC observations (Callies et al. 2014, hereafter C14; L15).

The B14 and L15 approaches follow from relations between the longitudinal–transverse and Helmholtz decompositions, which in turn require strong assumptions on the underlying flow, namely, horizontal homogeneity and isotropy. In the real atmosphere, these assumptions of course hold only approximately, and the two approaches may be relatively more or less sensitive to violations of the assumptions of homogeneity and isotropy. In this paper, we evaluate the accuracy of the B14 and L15 approaches for realistic flows by applying them to numerical output from the global atmospheric Model for Prediction Across Scales (MPAS; Skamarock et al. 2012), where the decomposition of the velocity into rotational and divergent components may be done unambiguously. When applied to aircraft observations (as in C14 and L15), these techniques require an additional assumption, which we do not test here: namely, that measured velocity time series can be converted to spatial transects using the mean airspeed of the plane.

The comparison of the two approaches presented in this manuscript is also motivated by the different ratios of divergent to rotational spectral energy on the mesoscales that have been found when applying the B14 and L15 implementations to MOZAIC data. C14 apply the B14 approach and find that velocity spectra at the mesoscales are dominated by the divergent contribution, which leads them to the conclusion that inertia–gravity waves likely account for the mesoscale energy spectrum. Contrarily, L15 finds the opposite result, with mesoscale spectra dominated by the rotational contribution, and concludes that inertia–gravity waves can be ruled out as important to the atmospheric mesoscale energy spectrum. Besides the differences in the details of their implementations, C14 and L15 also make different choices in their handling and processing of the observations. Thus, we also explore the sensitivity of the decomposition to some of these choices in the context of numerical simulations, though we do not attempt a detailed reconstruction of either study.

The paper is structured as follows: In section 2, the configuration of MPAS and the simulated period, the procedure of the spectral calculations, and the B14 and L15 approaches are described. The results of this study for global data are presented in section 3. General features of the kinetic, rotational, and divergent energy spectra in MPAS are reviewed, and the estimates of the respective energy components by B14 and L15 and the according errors are discussed. In section 4, we show that the different results of C14 and L15 for the dominance of rotational or divergent energies on the mesoscales in the MOZAIC data can be qualitatively reproduced by considering different subsets of the MPAS data. This paper concludes with a summary in section 5.

2. Data and methods

We test the B14 and L15 approaches by applying them to output from global atmospheric simulations. This section describes the numerical simulations, the various spectra that we compute from them, and the B14 and L15 implementations of the decomposition method.

a. The numerical simulation and computation of its spectra

To test the B14 and L15 approaches, we use output produced by the fully compressible nonhydrostatic atmospheric global MPAS, which is described in detail in Skamarock et al. (2012). The MPAS solver is discretized on a spherical centroidal Voronoi mesh. The results presented in this paper are computed over days 5–14 of a 15-day MPAS simulation initialized at 0000 UTC 15 January 2009, using a quasi-uniform mesh with an average cell-center spacing of 15 km. Spectra from the model generally spin up within 18 h, and omitting the first 5 days of simulations ensures that our results are not influenced by such spinup. The simulation is identical to the 15-km simulation of S14, and a detailed description of the model configuration, the physical parameterizations, the integration scheme, and the numerical diffusion used can be found there.

The B14 and L15 approaches provide estimates of the spectra of rotational and divergent energy, using one-dimensional power spectra of across- and along-track wind velocities as input. We will denote these spectra by $E_R(p)$, $E_D(p)$, $E_T(p)$, and $E_L(p)$, respectively, where p is the along-track wavenumber. In the present study, those spectra are calculated from the MPAS output as follows: The data is available on an unstructured grid that lacks a global coordinate system and is in a first step interpolated to a regular latitude–longitude grid. To that end, the Delaunay triangular mesh as the dual of the Voronoi mesh is used, and barycentric interpolation is used within the Delaunay triangle that contains a given latitude–longitude point (as described in S14). This interpolation is performed on the interpolated height levels 8.5, 9.5, 10.5, 16, 17, and 18 km, where model height surfaces are considered almost horizontal. Tropospheric results (TROP) are averaged over the first three levels, and stratospheric heights (STRAT) are averaged over the last three levels. As a second step, the gridded one-dimensional transects are extracted from the model output along constant latitude or longitude, and these are rendered periodic following Errico (1985). A discrete one-dimensional Fourier transform is then applied along the transects, and the resulting spectra are averaged over all longitudes or latitudes, respectively. All spectra displayed as a function of longitudinal wavenumber k will result from one-dimensional Fourier transforms taken along circles of constant latitude averaged over all latitudes. A dependence on the latitudinal wavenumber l will indicate that spectra have been calculated along circles of constant latitudes and along constant longitudes and averaged (scales larger than the minimum l are neglected in k spectra). All spectra presented in this paper are computed at 6-hourly intervals and further averaged over the 10 days of simulation (40 time slots in total).

To compare the results of B14 and L15 to E_R and E_D obtained from full model output, the velocity field is decomposed globally into rotational and divergent contributions. To that end, a spherical harmonics transform is applied to the fields of vertical vorticity and horizontal divergence on the regular latitude–longitude grid. The associated spectral representation of the streamfunction and the velocity potential and of the rotational and divergent components of the horizontal wind can then be easily calculated, and an inverse spherical harmonic transform gives the rotational and divergent wind components in real space. Those fields are then detrended in the latitudinal direction (even for global data the latitude range is restricted; see explanation below), and a two-dimensional Fourier transform is applied. To obtain a one-dimensional spectrum as a function of the along-track wavenumber, a direction for the one-dimensional spectrum (either latitudinal or longitudinal) is chosen, and the squared absolute values of the Fourier coefficients for both along- and across-track velocities are summed over the wavenumber in the across-track direction.

When taking discrete Fourier transforms of one-dimensional transects along circles of constant latitude of the interpolated regular latitude–longitude grid, issues related to the stretching of segments at higher latitudes to longer physical distances will arise. We have checked the influence of this geometric effect by comparing results from spectral calculations on the full, global latitude–longitude grid (including regions at high latitudes, where the effect is expected to be significantly more pronounced) to those from a grid restricted to latitudes between 60°S and 60°N. Comparing the obtained spectra with spectra computed from spherical harmonic coefficients for the full global fields, however, indicates that this effect changes neither the results nor the performance of the method qualitatively. The results shown in the present study are nevertheless restricted to the latitude range 60°S–60°N to assure that the geometric effect near the poles is neglected.

b. The Bühler and Lindborg approaches

On the sphere, the two-dimensional Helmholtz decomposition allows for the representation of any horizontal flow field $\boldsymbol{v}$ in terms of components associated with the divergence and the rotation of the flow. It reads

$$\boldsymbol{v} = \boldsymbol{v}_R + \boldsymbol{v}_D = -\nabla \times (\mathbf{e}_z \psi) + \nabla \phi ,$$

where $\boldsymbol{v}_R$ and $\boldsymbol{v}_D$ are the rotational and divergent wind components, $\boldsymbol{\nabla}$ denotes the horizontal gradient operator, $\mathbf{e}_z$ is the vertical unit vector, and ψ and ϕ are the streamfunction and velocity potential, respectively. All velocity components are defined in the x–y plane with associated wavenumbers p and q (in order to avoid confusion with the wavenumbers k and l that will denote longitudinal and latitudinal wavenumbers in the MPAS data), where x is the along-track direction. Furthermore, the altitude z and the time t are considered constant. Apart from the decomposition into rotational and divergent modes, a horizontal flow field sampled along a one-dimensional flight track can also be regarded as composed of an along- and across-track wind component, $\boldsymbol{v}_L$ and $\boldsymbol{v}_T$. The one-dimensional kinetic energy spectrum $E_K(p)$ can thus be expressed as

$$E_K(p) = E_T(p) + E_L(p) = E_D(p) + E_R(p) . \tag{1}$$

The p dependence of one-dimensional spectral quantities will be omitted in the following text for simplicity. Dependencies other than on p will be denoted explicitly. Assuming the flow is horizontally homogeneous and isotropic, and given the unique and exact decomposition [(1)], then E_R and E_D can be related to E_T and E_L. The equations from B14 and L15, given in the next sections, are mathematically equivalent formulations of these relations and thus the B14 and L15 approaches can be considered different implementations of the same method.

1) THE BÜHLER APPROACH

Under the assumption that the streamfunction ψ and velocity potential ϕ are isotropic random functions, B14 derive relationships between E_L and E_T and the two-dimensional isotropic spectra of ψ and ϕ. The resulting coupled ordinary differential equations (ODEs) take a simpler form when the y derivatives of the velocity potential and streamfunction spectra D^ϕ and D^ψ are introduced as auxiliary functions, with the result

$$p \frac{d}{dp} D^\psi(p) = D^\phi(p) - E_T(p) , \tag{2}$$

$$p \frac{d}{dp} D^\phi(p) = D^\psi(p) - E_L(p) , \tag{3}$$

where the subscripts L and T denote quantities derived from along- and across-track wind velocities as before.

We solve the ODE system (2) and (3) for D^ψ and D^ϕ numerically under the boundary condition that D^ψ and D^ϕ tend to zero for $p \to \infty$. Note that B14 also suggest a closed form solution, which implies the interpolation of the input E_L and E_T spectra to a logarithmic grid. However, to avoid the potential errors arising from this additional step, we chose to solve (2) and (3) numerically on the regular p grid. The required amount of smoothing depends on the level of noise in the data (i.e., sample size), and we find an averaging over wavenumber bins of width $5 \times 10^{-8}\,\mathrm{m}^{-1}$ to be sufficient for our data.

Adding (2) and (3) and regrouping the terms to components only associated with the streamfunction or velocity potential leads to the kinetic energy spectra of rotational and divergent winds:

$$E_R(p) = D^\psi(p) - p \frac{d}{dp} D^\psi(p) , \tag{4}$$

$$E_D(p) = D^\phi(p) - p \frac{d}{dp} D^\phi(p) , \tag{5}$$

where the subscripts R and D denote quantities derived from rotational and divergent wind velocities [see (2.27) in B14]. Note that the boundary condition that D^ψ and D^ϕ tend to zero for $p \to \infty$ implies that E_R and E_D tend to zero for largest wavenumbers. The described additional smoothing of the input E_L and E_T spectra has a negligible impact on the results (see section 3b).

2) THE LINDBORG APPROACH

The original approach of L07 begins from relationships between the two-point correlation function of vertical vorticity and horizontal divergence and the along- and across-track velocity correlation. As in B14, statistical isotropy and homogeneity are assumed. The desired relationships between the longitudinal-transverse and Helmholtz decompositions are derived in L07, but the calculation of the two-point correlation functions of vertical vorticity and horizontal divergence involves second-order differentiation of measurement data, leaving the estimate sensitive to noise.

L15 revisits the formulas found in L07 and derives two coupled ODEs that relate the two-point correlation functions of rotational and divergent velocities (R_{rr} and R_{dd}) to the correlation of longitudinal and transverse velocities (R_{ll} and R_{tt}). Under the boundary condition that the correlation functions tend to zero for infinite separation distances r, the respective relationships can be integrated over r, and L15 finds

$$R_{\mathrm{rr}} = R_{\mathrm{tt}} - \int_r^\infty \frac{1}{r}(R_{\mathrm{tt}} - R_{\mathrm{ll}})\,dr,$$

$$R_{\mathrm{dd}} = R_{\mathrm{ll}} + \int_r^\infty \frac{1}{r}(R_{\mathrm{tt}} - R_{\mathrm{ll}})\,dr.$$

Using the relation between structure functions and spectra for isotropic, homogeneous fields then gives formulas relating the rotational and divergent energy spectra to the spectra of horizontal wind velocities [(2.11) and (2.12) in L15]:

$$E_R(p) = E_T(p) + \frac{1}{p}\int_p^\infty [E_T(p) - E_L(p)]\,dp, \qquad (6)$$

$$E_D(p) = E_L(p) - \frac{1}{p}\int_p^\infty [E_T(p) - E_L(p)]\,dp, \qquad (7)$$

where definitions are as before. The relationships established by L15 relate E_R and E_D to E_L and E_T in a simpler way than L07 and B14 and can be implemented with a simple trapezoidal rule, where no preprocessing of the input data is necessary. For comparison with the B14 approach, the spectral equations [(6) and (7)] will be examined in the present study.

3. Spectra obtained from global data

In the following, we first discuss general characteristics of E_K, E_D, and E_R as calculated from MPAS data (i.e., two-dimensional fields). Use of $E^B_{D,R}$ refers to results obtained from solving (4) and (5) (as derived in B14) numerically, and $E^L_{D,R}$ are calculated from (6) and (7) using a trapezoidal rule, as in L15. Quantities without the superscript L or B refer to results obtained from the two-dimensional data and are then compared to the respective $E^{B,L}_{D,R}$. In a third part, the large-scale error of the two approaches is assessed.

The values of E_K, E_D, and E_R calculated for the considered period of time have already been presented in S14. S14 discuss in detail the fully global results of MPAS simulations with 3-km horizontal resolution, as opposed to this study, where 15-km data are calculated on a narrower latitude band (60°S–60°N) and rendered periodic in latitudinal direction. S14 furthermore use a global spherical harmonic decomposition and a summation over spherical harmonics with the same total wavenumber. Since the data used in the current study are on a limited area, we use a two-dimensional Fourier transform on the fields, and results are displayed as a function of along-track wavenumber for comparability with the B14 and L15 studies. The S14 methodology for the calculation of one-dimensional spectra is thus slightly different from our approach, and we will briefly review general features of the spectra.

a. *General features of the spectra*

In Fig. 1 E_K is displayed as a function of longitudinal wavenumber k as a red line for TROP (left) and STRAT (right). As in S14, the observed features of the atmospheric energy spectrum, with a −3 scaling at larger scales that merges into a shallower spectrum for scales smaller than around 500 km, are well reproduced in both height regimes. The model's accurate reproduction of the flow on small scales is bounded by the effective resolution (i.e., the scale at which model filter effects become important). From a comparison with higher-resolved MPAS simulations, S14 estimate the effective resolution of the model in this configuration as 4–6 times the horizontal grid spacing Δ (solid gray vertical lines in Fig. 1). Thus, spectra for the evaluated MPAS data will not be considered accurate on scales smaller than 100 km, and the term "mesoscales" will, in the following, refer to the wavelength range from 100 to 1000 km. As discussed in previous modeling studies (e.g., Hamilton et al. 2008), the shallowing of E_K on largest (global) scales is considered a physical feature of the energy spectrum of the real atmosphere (Boer and Shepherd 1983) but should be interpreted with care, since the shape of the spectrum results from an average over a few Fourier modes and is thus highly variable.

As seen in S14, the mesoscale transition (i.e., the scale where the shape of the E_K spectrum changes from a steeper synoptic scale to a shallower mesoscale slope) is at somewhat longer wavelengths in STRAT (600–800 km) than in TROP (300–500 km). This shift of the transition to larger scales with height is consistent with previous studies with global models (Koshyk and Hamilton 2001; Burgess et al. 2013) and with idealized simulations of baroclinic waves (Waite and Snyder 2013). It appears to arise from upward-propagating inertia–gravity waves, where the divergent component of the flow maintains its amplitude, while the rotational component decays.

In Fig. 2, the fraction of E_D of E_K is displayed in percentage terms as a function of longitudinal wavenumber for TROP (left) and STRAT (right). In TROP, E_R dominates E_K for all wavenumbers. For scales larger than 1000 km, E_D amounts to about 10% of E_K. The

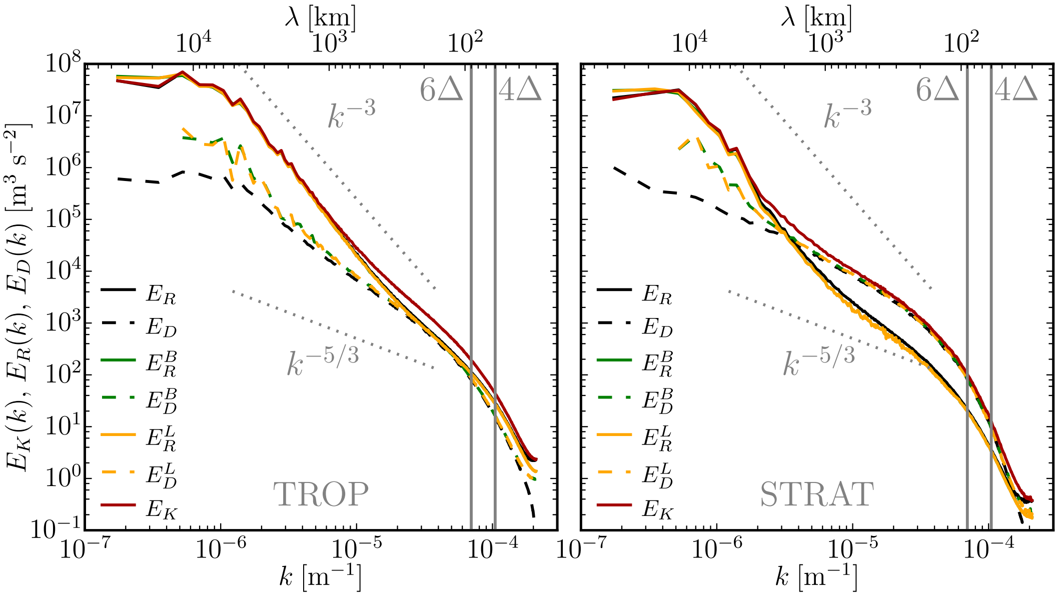

FIG. 1. Plots of E_K, E_R, and E_D, as calculated from the full MPAS dataset, and $E_{D,R}^{B,L}$ for (left) TROP and (right) STRAT as a function of k in double logarithmic space. The spectra are taken along longitudinal bands and then averaged over latitudes between 60°S and 60°N.

associated dominance of E_R leads to the observed -3 wavenumber dependence of E_K on the large scales. From Fig. 1, it can be seen that the E_D spectrum features a significantly shallower slope (closer to $-5/3$). On the mesoscales, the contribution of E_D to E_K increases with decreasing scale and accounts for up to 45% of E_K, with an average ratio $E_D/E_R \approx 0.7$. In contrast, the STRAT mesoscales are characterized by a dominance of divergent motions, where E_D makes up 80% of E_K on scales of a couple hundreds of kilometers. The STRAT E_R and E_D spectra cross at a scale of around 2000 km, leading to a sharper mesoscale transition that occurs at longer wavelengths than in TROP. The mean mesoscale (i.e., averaged over all wavenumbers in the mesoscale range 100–1000 km) ratio E_D/E_R is found to be 4.1.

Previous modeling studies disagree concerning the ratio of E_D to E_R on the atmospheric mesoscales. As in our study, S14 find an equipartition of energy between E_D and E_R in the upper-tropospheric mesoscales; earlier studies, such as Koshyk and Hamilton (2001), hint at a similar result, though they do not resolve the majority of the mesoscale range. Blažica et al. (2013) examine the height dependence of the contribution of divergent to kinetic energy in the numerical weather prediction model ALADIN and find that divergent energy amounts to about 50% of kinetic energy in the free troposphere. Hamilton et al. (2008), in contrast, find in simulations of a high-resolution GCM that, near the tropopause, the rotational dominates over the divergent energy on the mesoscales, with $E_R \approx 4E_D$. In the stratosphere, model simulations generally agree that transition to a flatter mesoscale spectrum occurs at larger scales than in the troposphere and that E_D increases relative to E_R (Koshyk and Hamilton 2001; Hamilton et al. 2008; Blažica et al. 2013; Burgess et al. 2013; Waite and Snyder 2013; S14). Several studies (Koshyk and Hamilton 2001; Burgess et al. 2013; Waite and Snyder 2013) attribute these characteristics of the stratospheric energy spectrum to mesoscale inertia–gravity waves propagating upward from the troposphere, though Augier and Lindborg (2013) compare the spectral energy budgets in two different models and show that vertical propagation of mesoscale waves is important in only one of them.

b. *Estimate from B14 and L15*

In Fig. 1, $E_D^{B,L}$ and $E_R^{B,L}$ are displayed as green and yellow lines. The two approaches produce almost identical results and work very well. Because of the different solution technique and the required smoothness of the input data, $E_{D,R}^B$ are marginally smoother than $E_{D,R}^L$. When plotted on a traditional log–log scale, the results are almost indistinguishable from the correct answer (black lines). The underlying mathematical assumptions of isotropy and homogeneity must be well satisfied, at least when data are aggregated over large areas.

The absolute errors of B14 and L15 are displayed in Fig. 3. The error is defined as the absolute value of the

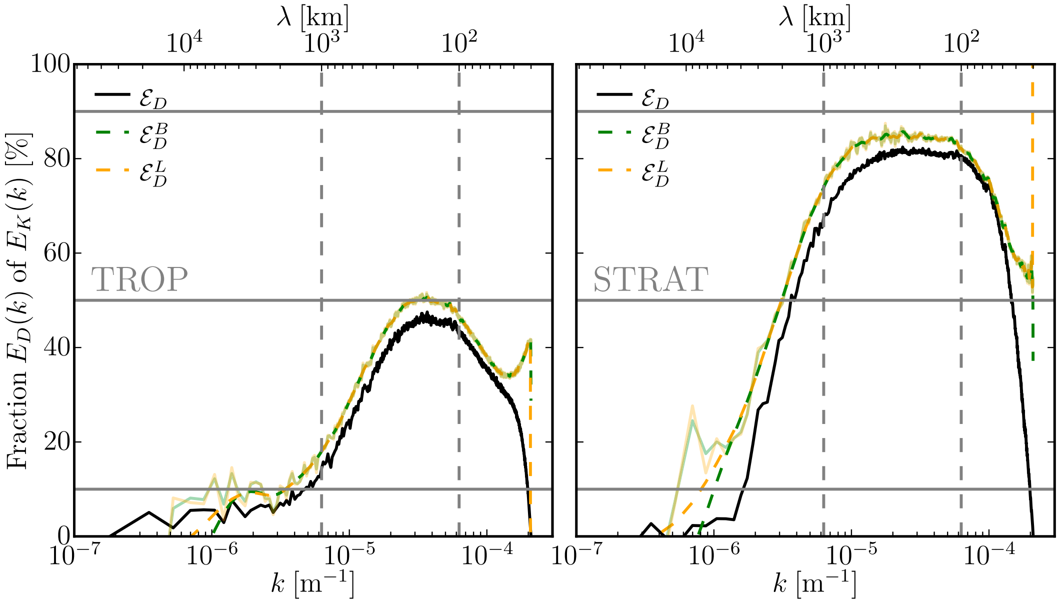

FIG. 2. Fraction of E_D of E_K (%) from Fig. 1 for (left) TROP and (right) STRAT. Solid gray horizontal lines demark 10%, 50%, and 90%; dashed vertical gray lines indicate horizontal scales of 100 and 1000 km for orientation. Dashed green and yellow lines are moving averages over three wavenumber bins of associated opaque solid lines.

difference between $E_D^{B,L}$ and $E_R^{B,L}$ and the corresponding energy component from MPAS data, normalized by the latter, and it provides a quantitative view on the quality of the estimates of B14 and L15. Mean mesoscale errors of $E_D^{B,L}$ and $E_R^{B,L}$ amount to 11.0% and 7.2% (TROP) and 4.7% and 17.7% (STRAT), respectively. The largest errors are found in $E_D^{B,L}$ on the largest scales and in both energy components near the grid scale. It furthermore appears that the smaller energy component is estimated systematically worse. In Fig. 1, $E_D^{B,L}$ takes negative values for the two largest Fourier modes and is thus not displayed on the log–log-scaled plot. L15 also noticed this unphysical behavior, and we will take up this issue in section 3c. The errors on the small-scale end of the spectra in Fig. 1 arise for Fourier modes on the grid scale. Because, as pointed out before, evaluated MPAS spectra are not accurate on scales smaller than 100 km as a result of the strong impact of model filter effects, we will not discuss these errors further.

In Fig. 2, the ratio E_D/E_K is displayed for TROP (left) and STRAT (right). The discussed errors are, in fact, small enough that the ratio is also estimated well with values $E_D^{B,L}/E_K^{B,L} \approx 0.9$ in TROP and 5.2 in STRAT (compared to 0.7 and 4.1, respectively, in the MPAS data). The B14 and L15 techniques should thus be able to provide a strong observational check on the mesoscale behavior of numerical models. As will be discussed in section 4, however, careful attention must be paid to which subset (i.e., latitude and height) of observations is considered.

c. *Assessment of errors*

A striking feature of Figs. 1 and 3 is the relatively large error of $E_D^{B,L}$ on large scales. This might result from violation of the underlying assumptions of B14 and L15 (see section 2b), but another possibility is that, because of the small amplitude of E_D relative to E_R, $E_D^{B,L}$ may be contaminated by small noise in E_R. We address this issue by calculating $E_D^{B,L}$ as in section 3b, but beginning from either purely rotational ($\boldsymbol{v} = \boldsymbol{v}_R$) or purely divergent ($\boldsymbol{v} = \boldsymbol{v}_D$) components of the original MPAS velocities. If the large-scale error of $E_D^{B,L}$ is related to a bad signal-to-noise ratio, it is expected to be significantly reduced for the purely divergent flow.

In Fig. 4, $E_{D,R}$ and $E_{D,R}^L$ are displayed for scales larger than ~1000 km for the full flow field (as Fig. 1) and E_D^L from $\boldsymbol{v}_D$ alone or $\boldsymbol{v}_R$ alone. All estimates of the B14 technique are quantitatively and qualitatively almost identical to the corresponding L15 estimates and are not shown for reasons of clarity. As discussed in section 3b, the difference between $E_D^{B,L}$ and E_D grows with increasing scale in TROP and STRAT (see black and yellow dashed lines in Fig. 4). When computed from $\boldsymbol{v}_R$ alone (dashed green line), E_D^L qualitatively resembles the estimate from the full flow field (dashed yellow line). Note especially that

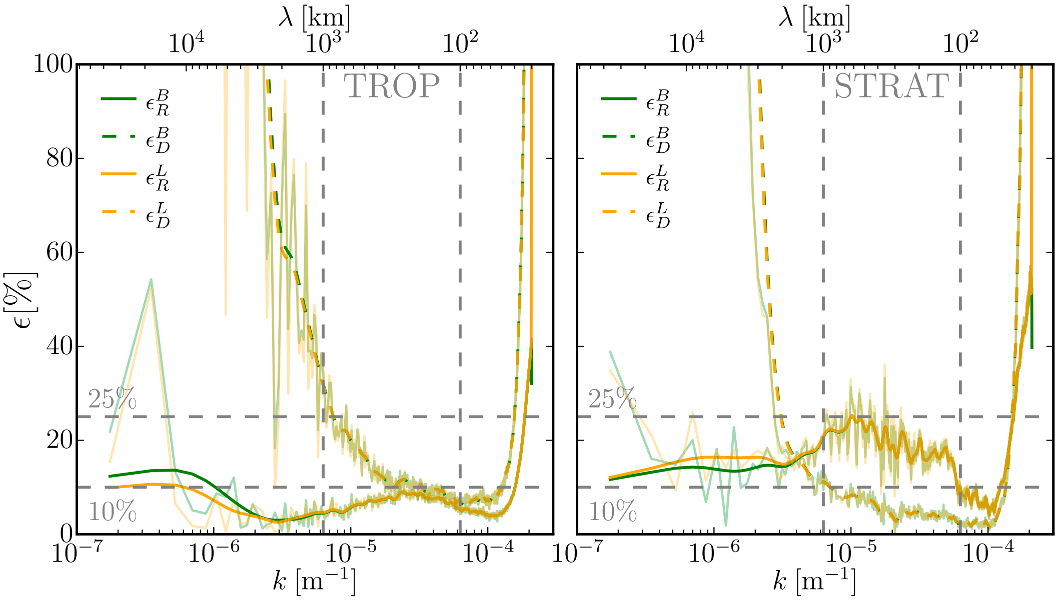

FIG. 3. Absolute error ε (%) of $E_{D,R}^{B,L}$ from Fig. 1 for (left) TROP and (right) STRAT. Gray horizontal lines indicate 10% and 25%; moving averages are calculated as in Fig. 2.

$E_D^{B,L}$ is estimated with significant amplitude, although the divergent wind is set to zero in the input data. The value of $E_D^{B,L}$ computed from $\boldsymbol{v}_D$ alone (dashed red line), however, compares significantly better to E_D. These results clearly show that the poor retrieval of E_D by B14 and L15 on large scales is related to a bad signal-to-noise ratio: the big error of $E_D^{B,L}$ is caused by small errors in E_R on large scales that contaminate the divergent component, which is small compared to the rotational component, and not by errors arising from violations of the underlying assumptions about the flow, such as isotropy and homogeneity.

An analogous test of the dependence of errors of the E_R estimate from either $\boldsymbol{v}_R$ or $\boldsymbol{v}_D$ alone (not shown) does not give results as clear as those for E_D. The error of the E_R estimate is, in particular, neither in general

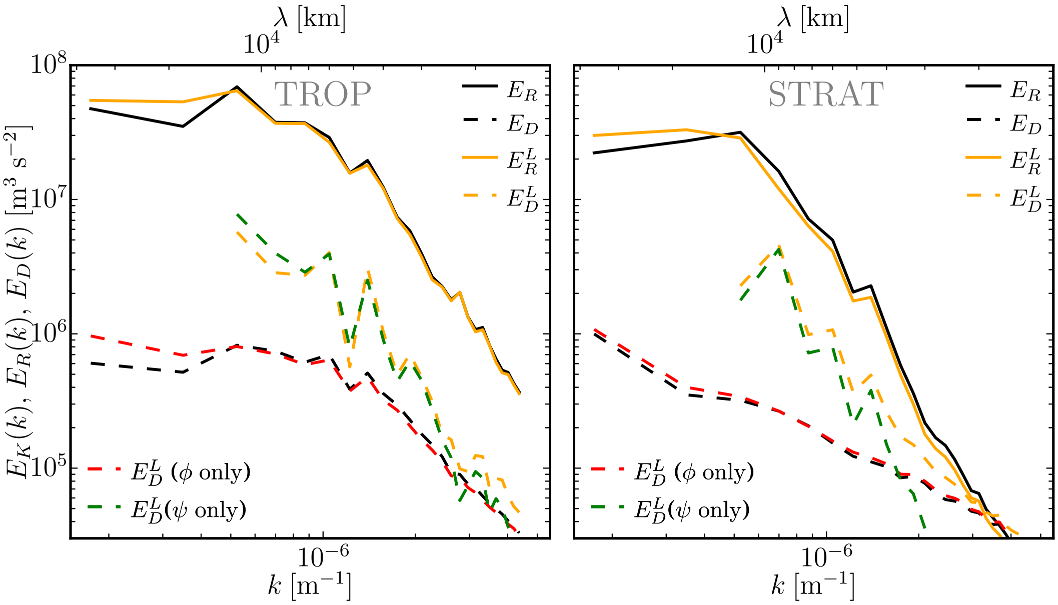

FIG. 4. Plots of E_R and E_D, as calculated from the full MPAS dataset, and $E_{D,R}^L$ from the full flow field as well as $E_{D,R}^L$ from $\boldsymbol{v}_D$ alone or $\boldsymbol{v}_R$ alone for (left) TROP and (right) STRAT. Scales larger than ~1000 km are shown.

nor on a certain scale range drastically reduced if E_R is computed from $\boldsymbol{v}_R$ alone. This points to other error sources being more relevant to the E_R estimate than the signal-to-noise ratio. This issue warrants further investigation.

4. Exploring the results of C14 and L15

C14 and L15 applied the B14 and L15 approaches, respectively, to the global MOZAIC commercial aircraft dataset. They found different ratios E_D/E_R on the atmospheric mesoscales and drew differing conclusions regarding the dominant dynamical character on this scale range. In this section, the different results of C14 and L15 are discussed in the framework of the MPAS data.

a. Comparing C14 and L15

C14 find from the application of B14 to MOZAIC data that the rotational component dominates the energy spectrum on the synoptic scales and that E_D becomes of the same order of magnitude as E_R near the transition scale. On the mesoscales, C14 find a slight dominance of E_D over E_R. The authors conclude from this that mesoscale dynamics are governed by unbalanced ageostrophic inertia–gravity wave (IGW) motions and that the transition in the E_K spectrum originates from IGWs becoming dominant on the respective scales. According to C14, an IGW field that is dominated by near-inertial waves is expected to feature a ratio $E_D/E_R \approx \omega^2/f^2$ of about unity (with Coriolis parameter f and frequency ω). The dynamic picture that emerges from the C14 results is a forward enstrophy cascade forced by geostrophic synoptic-scale baroclinic disturbances, which is masked by inertia–gravity waves for scales smaller than about 500 km.

In contrast, L15 finds, based on a structure function analysis of MOZAIC data, that E_R dominates over E_D on the mesoscales at all heights and with largest values $E_D/E_R \approx 0.33$ in the upper troposphere. Arguing that any realistic IGW frequency distribution features a ratio E_D/E_R significantly larger than unity, L15 concludes that gravity waves can be ruled out as being the major dynamical feature leading to the observed atmospheric energy spectrum.

There are two potential causes for the disagreement between the C14 and L15 results: First, the different results can arise from different estimates $E_{D,R}^{B,L}$ from given E_T and E_L (i.e., there are inherent limitations to the accuracy of the diagnostic methods). This possibility is ruled out by the results of section 3b. In what follows, we examine the second possibility: that the difference between the results of C14 and L15 arises from differences in their processing of the MOZAIC measurement data.

C14 use MOZAIC data obtained in 2002–10 and utilize only flight segments that are longer than 6000 km and lie completely in the Northern Hemispheric midlatitudes (30°–60°N). These criteria reduce the number of evaluated segments to 458 and select mainly flights that are more or less along tracks at constant latitude. The data are not separated into upper-tropospheric and lower-stratospheric portions; rather, all flight levels are averaged together.

L15 uses the 1994–97 MOZAIC dataset without restrictions concerning the segment length (leading to a smaller evaluated scale range than in C14) or location of the flight track. The resulting 7630 randomly oriented flight segments are separated according to ozone levels into nominally tropospheric ($<$100 ppbv) and stratospheric ($>$200 ppbv) heights and averaged globally.

b. MPAS results

Since C14 and L15 use different subsets of the MOZAIC data, their different conclusions with regard to the mesoscale ratio E_D/E_R are not necessarily contradictory. By evaluating only long flights in a narrow latitude band, C14 only include spectra with a longitudinal wavenumber dependence in a rather homogeneous flow field. The discussion of the vertical dependence of E_D/E_R and the transition scale from synoptic to mesoscale flow regimes in section 3a further indicates that averaging over tropospheric and stratospheric height regions might lead to different results than separating those heights. Furthermore, L15 averages over 16 times more flight segments, which are more randomly oriented and distributed over the globe. This might render the evaluated data more isotropic and smooth. The latitudinal dependence of energy spectra and the accuracy of the isotropy assumption on the flow (Nastrom and Gage 1985; Cho and Lindborg 2001) might also lead to different results when spectra are averaged over the globe, as opposed to a narrow latitudinal band.

We next compare spectral shapes and estimates of E_D/E_R computed by applying the B14 or L15 techniques to subsets of the MPAS data that mimic those used by C14 and L15. To mimic the C14 setup, one-dimensional spectra are taken along constant latitudes and averaged over latitudes in the range 30°–60°N and TROP (C14 setup). For the L15 setup, the input spectra are calculated globally along bands of constant latitude and longitude and averaged separately for TROP and STRAT. Note that, for the L15 setup, the resulting spectra are displayed over a smaller range of wavenumbers, since the latitudinal tracks are shorter than the longitudinal.

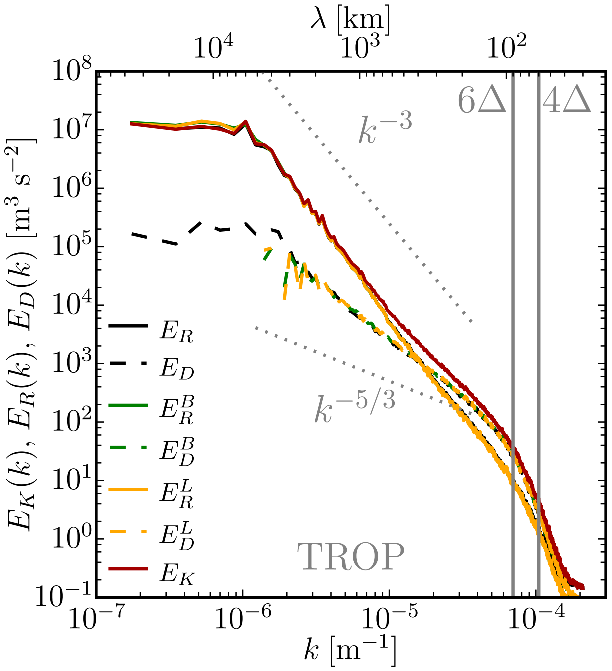

FIG. 5. As in Fig. 1, but for the C14 setup.

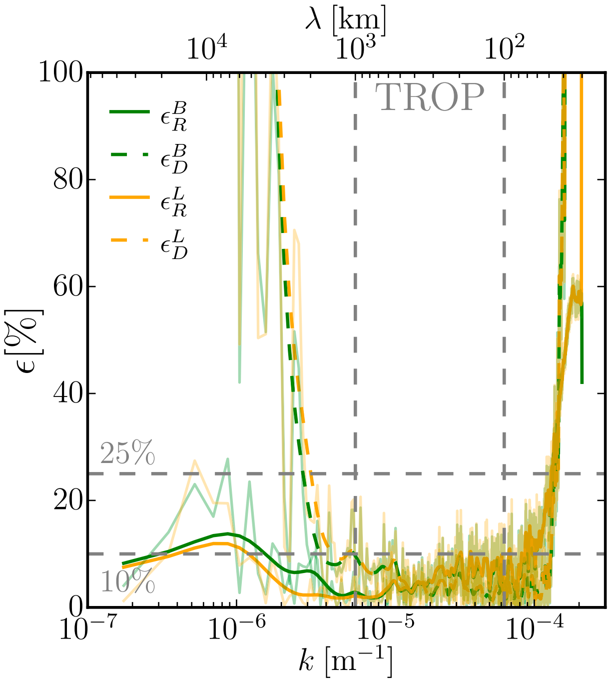

FIG. 6. As in Fig. 3, but for the C14 setup.

Figure 5 displays E_K, E_D, and E_R for the full MPAS data, as well as $E_{D,R}^{B,L}$ for the C14 setup. Note that E_D dominates over E_R up to a transition scale at around 400–500 km. Beyond that scale, the spectra cross, and E_R dominates E_D for larger scales. The scale where E_R and E_D cross also marks the transition of the E_K spectrum from a shallower mesoscale slope to a steeper slope on synoptic scales. This agrees well with the transition scale of 500 km found by C14.

Figure 5 shows $E_{D,R}^{B,L}$, and their errors, as defined in section 3b, are displayed in Fig. 6. As before, the approaches show matching results and error dependence on along-track wavenumber. We see that $E_D^{B,L}$ compares well to E_D up to a certain scale (here around 2000 km) and then becomes very noisy and takes nonphysical negative values on the largest scales (see section 3c). The errors of $E_D^{B,L}$ and $E_R^{B,L}$ show, in contrast to the global data, no variation with scale and take small mean mesoscale values of 6.2% ($E_R^{B,L}$) and 3.8% ($E_D^{B,L}$).

The contribution of E_D to E_K is displayed in percentage terms in Fig. 7. For MPAS data, the fraction of E_D to E_K gradually drops from roughly 70% at scales near 100 km to 50% at 400–500 km. The mean ratio E_D/E_R amounts to 1.8 on the mesoscales.

The results based on the full MPAS data as well as $E_{D,R}^{B,L}$ reproduce the dominance of E_D over E_R on the mesoscale in the C14 setup. While the MPAS data feature $E_D/E_R \approx 1.8$ on the mesoscales, B14 and L15 estimate a value of 2.0 (as shown in Fig. 7). Note additionally that because of limitations in the height levels of the available MPAS data, the C14 setup only contains upper-tropospheric height levels

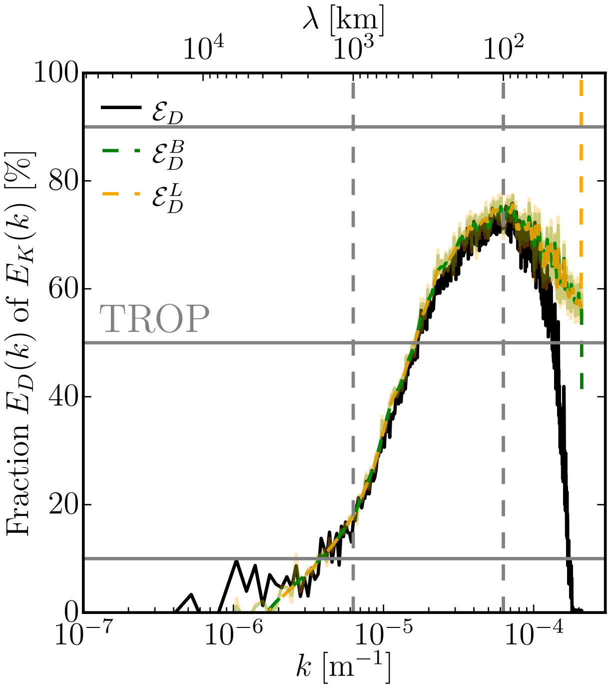

FIG. 7. As in Fig. 2, but for the C14 setup.

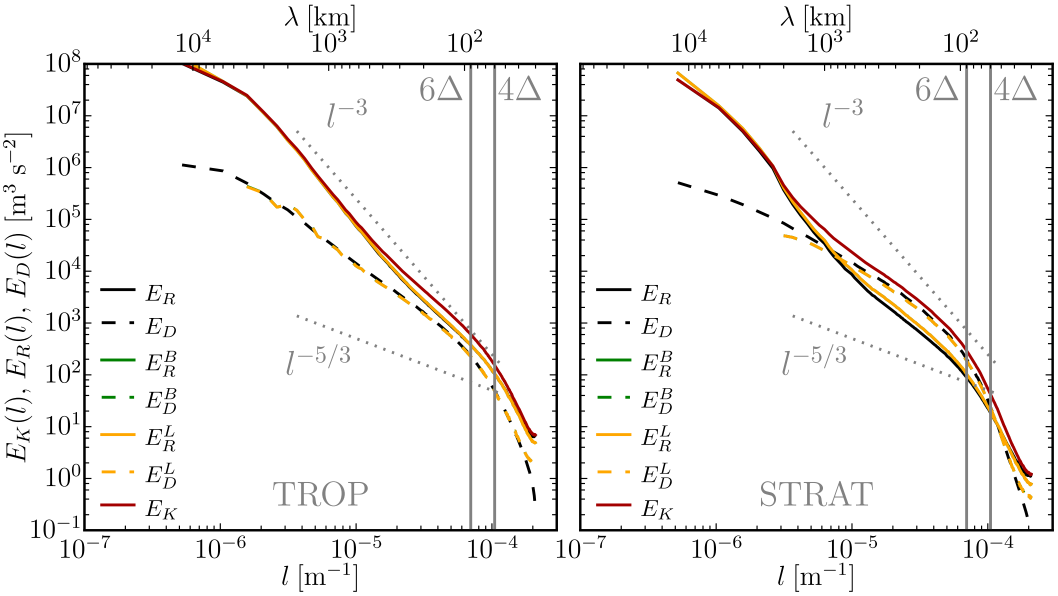

FIG. 8. As in Fig. 1, but for the L15 setup.

8.5, 9.5, and 10.5 km. Because of the increase of mesoscale E_D with increasing height, as reported in the current as well as earlier model studies, we expect the dominance of E_D on the mesoscales to be even more pronounced if lower-stratospheric data were included.

In Fig. 8, E_K, E_D, and E_R for full MPAS data and $E_{D,R}^{B,L}$ are displayed for the L15 setup and TROP (left) and STRAT (right). The TROP spectra calculated from MPAS data show a dominance of E_R over E_D across the entire scale range with an increasing dominance with increasing scale. Note that E_K again flattens from a steep synoptic scale to a shallower slope on the mesoscale. Contrarily, in STRAT, E_D dominates E_R on scales up to a horizontal scale of around 1000 km where the spectra cross. While E_D has a shallow slope close to a $-5/3$ wavenumber dependence, E_R features a steep approximately -3 dependence on horizontal wavenumber.

The errors according to $E_{D,R}^{B,L}$ shown in Fig. 8 are displayed in Fig. 9. In TROP, the errors for E_D and E_R do not exceed values of around 10% up to scales of 1000 km with mean values of 3.3% ($E_R^{B,L}$) and 6.7% ($E_D^{B,L}$) on the mesoscales. In STRAT, the errors of the estimate of E_D and E_R take significantly larger values than the previously discussed C14 and global data results. For the L15 setup, B14 and L15 find mean mesoscale ratios E_D/E_R of 0.5 (TROP) and 1.6 (STRAT).

The fraction E_D/E_K, as calculated from MPAS data as well as for the B14 and L15 estimates and TROP (left) and STRAT (right), is displayed in Fig. 10. In TROP, E_D contributes the most to E_K on scales of a few hundreds of kilometers (45%) and drops continuously to a couple of percent on scales around 1000 km. The mean mesoscale ratio E_D/E_R amounts to 0.5. In STRAT (right panel of Fig. 10), E_D dominates E_R on the mesoscales. On larger scales, the amplitude of E_D decreases rapidly with increasing scale. For the full MPAS data, the mean mesoscale ratio E_D/E_R is found to be 1.8. From Figs. 8 and 10, it is obvious that the dynamics governing the mesoscales differ significantly in tropospheric and stratospheric heights.

In summary, the mesoscale ratio E_D/E_R larger than unity found by C14 for vertically averaged MOZAIC data between 30° and 60°N is reproduced by the B14 and L15 approaches for a similar subset of MPAS data and the evaluated time span. Using global data averaged over spectra aligned along constant longitudes and latitudes, separating tropospheric and stratospheric heights with the available MPAS data, and applying the B14 and L15 approaches reproduces the L15 result of a dominance of mesoscale E_R over E_D. The errors for B14 and L15 in comparison with MPAS data are too small to account for differences in the dominance of E_D and E_R on the mesoscales. The divergent deductions drawn in C14 and L15 concerning the ratio E_D/E_R on the atmospheric mesoscales do not result from differences or limitations in the B14 and L15 approaches, but rather from the evaluation of different subsets of the MOZAIC data (especially averaging over different heights). This finding is furthermore supported by the mesoscale

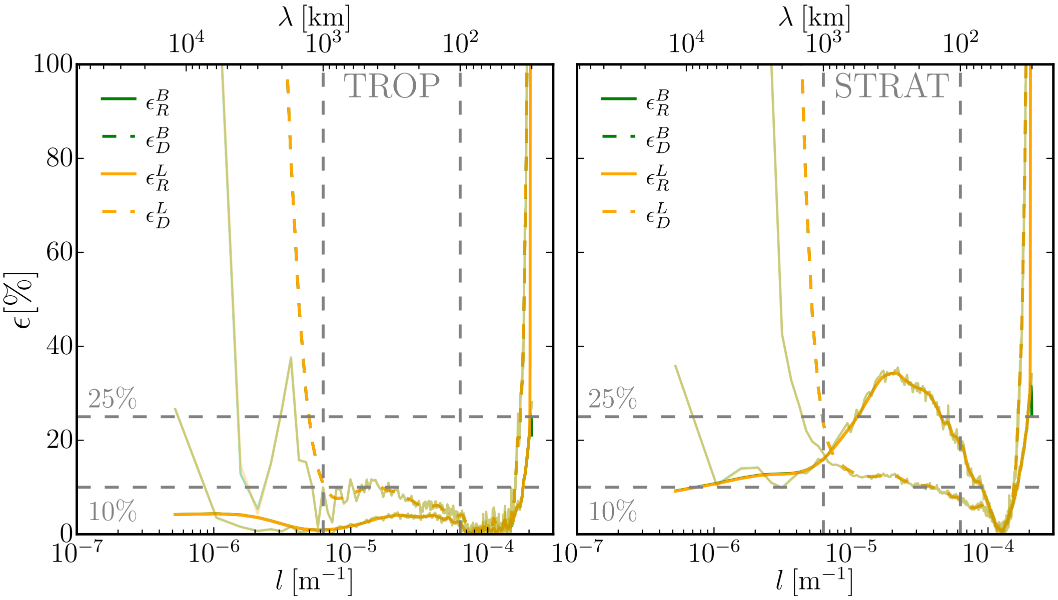

FIG. 9. As in Fig. 3, but for the L15 setup.

equipartition of E_D and E_R found by L07 for averaged tropospheric and stratospheric global data.

Differences in the spectra between the C14 and L15 setups arise mainly from variations in the mesoscale spectra with latitude. For TROP, the mesoscale energy is dominated by E_D in the Northern Hemisphere and tropics and E_R in the Southern Hemisphere (not shown). This result is in agreement with observational studies that find a dependence of mesoscale spectral variability on the latitudinal range (e.g., Nastrom et al. 1984). Considering transects only in the zonal or meridional direction has little effect (not shown).

5. Summary

We have evaluated two approaches (B14 and L15) for estimating rotational and divergent kinetic energy spectra from one-dimensional measurements of across- and

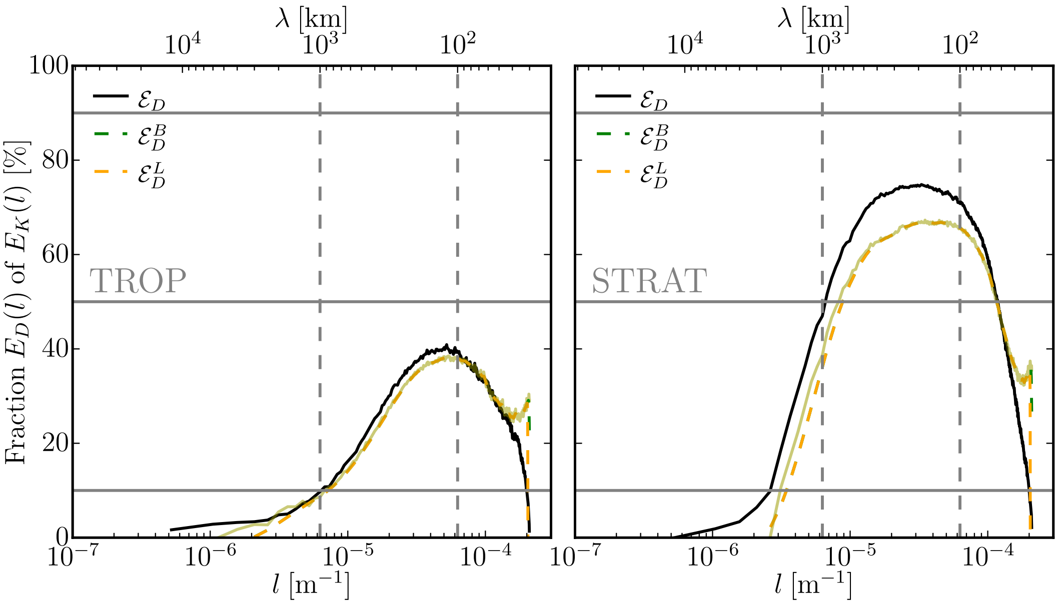

FIG. 10. As in Fig. 2, but for the L15 setup.

along-track wind components. Both approaches are based on relations between rotational or divergent spectra and velocity along one-dimensional tracks that follow when the flow is homogeneous and isotropic. While B14 requires prior smoothing of the data and the solution of a set of coupled ODEs, L15 is implemented with a simple trapezoidal rule for solving their equations without preprocessing of the data. One-dimensional transects of horizontal velocity fields simulated by the Model for Prediction Across Scales (MPAS) taken along circles of constant latitudes and longitudes serve as an input to the proposed approaches. The resulting spectra of divergent and kinetic energy are then compared to the respective spectra calculated from two-dimensional fields from MPAS, where the decomposition may be done unambiguously.

The two implementations of the decomposition method are very accurate and yield results almost indistinguishable from the correct solution when plotted on the traditional log–log scale. Their errors are largest for the divergent energy on the largest scales and for both energy components near the grid scale. At the mesoscale, errors are 11% and 7% for divergent and rotational components, respectively, in the troposphere and 5% and 18%, respectively, in the stratosphere. The errors on the small-scale end of the spectrum are not further discussed since they are on scales smaller than the effective resolution of the model. The large errors and the unphysical negative values of the estimate of the divergent kinetic energy component by both approaches are also found by L15. While L15 relates those errors to violations of large-scale isotropy, we find through an examination of purely divergent flows that the cause is most likely a contamination of the divergent kinetic energy estimate by small errors in the dominant rotational energy.

Attributing mesoscale errors and their variation with scale to the violation of certain underlying assumptions is not straightforward and is beyond the scope of this study. On the mesoscales, however, the errors of B14 and L15 are small enough that the mesoscale ratio of divergent to rotational kinetic energy (i.e., whether the flow is mainly governed by quasi-two-dimensional motions or inertia–gravity waves) can be estimated accurately. We thus conclude that, at least when data are aggregated over large areas, the underlying assumptions of isotropy and homogeneity must be well satisfied.

The application of the B14 and L15 approaches to MOZAIC data by C14 and L15 led to differing conclusions concerning the mesoscale ratio of divergent to rotational energy components. We assessed this issue by applying the B14 and L15 implementations to various subsets of the MPAS data. Although we did not attempt to reproduce either study in detail, a critical sensitivity of the results to the evaluated latitudinal and height range was found: Using upper-tropospheric transects aligned along circles of constant latitude in the range from 30° to 60°N gave a ratio of divergent to rotational energy of around 2, while averaging over transects along both constant latitudes and constant longitudes and separated into tropospheric and stratospheric heights showed an equipartition of rotational and divergent energy in the upper-tropospheric mesoscale.

This result is consistent with the much larger ratio of divergent to rotational energy found by C14 ($E_D/E_R \approx 2$) compared to that found by L15 ($E_D/E_R \approx 1/3$); C14 used long transects of MOZAIC data in the same latitudinal band averaged over upper-tropospheric and lower-stratospheric heights, while L15 considered transects with random orientation and length and separated data between upper-tropospheric and lower-stratospheric heights.

We conclude that the results of C14 and L15 differ not because of inherent limitations or differences in the approaches they use, but rather from their choices of which subset of the MOZAIC data to examine and the sensitivity of E_D/E_R to the selected latitude and height region. A corollary is that explanations of the dynamics underlying the mesoscale energy spectrum may vary between different regions of the atmosphere. Future studies that analyze those dynamics will need to account for such variations.

The nature of the mesoscale energy spectrum and its underlying dynamics have long been debated, and previous modeling and observational studies come to contradictory results concerning the main dynamical agent on the mesoscale. Our study shows that the techniques proposed by B14 and L15 provide a strong observational check of model results with existing large commercial aircraft datasets as long as care is taken in matching the height and latitude of the model data to that of the aircraft observations. The methods could thus yield an important contribution to understanding current research questions regarding the dynamical regime underlying the mesoscale energy spectrum, its variability, and associated error growth mechanisms (C14; Selz and Craig 2015).

Acknowledgments. Lotte Bierdel was supported by NCAR's Advanced Study Program during a collaborative visit to NCAR. The authors furthermore thank Rich Rotunno and three anonymous reviewers for their thoughtful comments on the manuscript.

REFERENCES

Augier, P., and E. Lindborg, 2013: A new formulation of the spectral energy budget of the atmosphere, with application to two high-resolution general circulation models. *J. Atmos. Sci.*, **70**, 2293–2308, doi:10.1175/JAS-D-12-0281.1.

Bacmeister, J. T., S. D. Eckermann, P. A. Newman, L. Lait, K. R. Chan, M. Loewenstein, M. H. Proffitt, and B. L. Gary, 1996: Stratospheric horizontal wavenumber spectra of winds, potential temperature, and atmospheric tracers observed by high-altitude aircraft. *J. Geophys. Res.*, **101**, 9441–9470, doi:10.1029/95JD03835.

Bierdel, L., P. Friederichs, and S. Bentzien, 2012: Spatial kinetic energy spectra in the convection-permitting limited-area NWP model COSMO-DE. *Meteor. Z.*, **21**, 245–258, doi:10.1127/0941-2948/2012/0319.

Blažica, V., N. Žagar, B. Strajnar, and J. Cedilnik, 2013: Rotational and divergent kinetic energy in the mesoscale model ALADIN. *Tellus*, **65A**, 18918, doi:10.3402/tellusa.v65i0.18918.

Boer, G., and T. Shepherd, 1983: Large-scale two-dimensional turbulence in the atmosphere. *J. Atmos. Sci.*, **40**, 164–184, doi:10.1175/1520-0469(1983)040<0164:LSTDTI>2.0.CO;2.

Brune, S., and E. Becker, 2013: Indications of stratified turbulence in a mechanistic GCM. *J. Atmos. Sci.*, **70**, 231–247, doi:10.1175/JAS-D-12-025.1.

Bühler, O., J. Callies, and R. Ferrari, 2014: Wave–vortex decomposition of one-dimensional ship-track data. *J. Fluid Mech.*, **756**, 1007–1026, doi:10.1017/jfm.2014.488.

Burgess, B. H., A. R. Erler, and T. G. Shepherd, 2013: The troposphere-to-stratosphere transition in kinetic energy spectra and nonlinear spectral fluxes as seen in ECMWF analyses. *J. Atmos. Sci.*, **70**, 669–687, doi:10.1175/JAS-D-12-0129.1.

Callies, J., R. Ferrari, and O. Bühler, 2014: Transition from geostrophic turbulence to inertia–gravity waves in the atmospheric energy spectrum. *Proc. Natl. Acad. Sci. USA*, **111**, 17 033–17 038, doi:10.1073/pnas.1410772111.

Charney, J. G., 1971: Geostrophic turbulence. *J. Atmos. Sci.*, **28**, 1087–1095, doi:10.1175/1520-0469(1971)028<1087:GT>2.0.CO;2.

Cho, J. Y. N., and E. Lindborg, 2001: Horizontal velocity structure functions in the upper troposphere and lower stratosphere: 1. Observations. *J. Geophys. Res.*, **106**, 10 223–10 232, doi:10.1029/2000JD900814.

——, R. E. Newell, and J. D. Barrick, 1999: Horizontal wavenumber spectra of winds, temperature, and trace gases during the Pacific Exploratory Missions: 2. Gravity waves, quasi-two-dimensional turbulence, and vortical modes. *J. Geophys. Res.*, **104**, 16 297–16 308, doi:10.1029/1999JD900068.

Dewan, E., 1997: Saturated-cascade similitude theory of gravity wave spectra. *J. Geophys. Res.*, **102**, 29 799–29 817, doi:10.1029/97JD02151.

Errico, R. M., 1985: Spectra computed from a limited area grid. *Mon. Wea. Rev.*, **113**, 1554–1562, doi:10.1175/1520-0493(1985)113<1554:SCFALA>2.0.CO;2.

Frehlich, R., and R. Sharman, 2008: The use of structure functions and spectra from numerical model output to determine effective model resolution. *Mon. Wea. Rev.*, **136**, 1537–1553, doi:10.1175/2007MWR2250.1.

Gage, K. S., 1979: Evidence for a $k^{-5/3}$ law inertial range in mesoscale two-dimensional turbulence. *J. Atmos. Sci.*, **36**, 1950–1954, doi:10.1175/1520-0469(1979)036<1950:EFALIR>2.0.CO;2.

——, and G. D. Nastrom, 1985: On the spectrum of atmospheric velocity fluctuations seen by MST/ST radar and their interpretation. *Radio Sci.*, **20**, 1339–1347, doi:10.1029/RS020i006p01339.

Gkioulekas, E., and K. K. Tung, 2006: Recent developments in understanding two-dimensional turbulence and the Nastrom–Gage spectrum. *J. Low Temp. Phys.*, **145**, 25–57, doi:10.1007/s10909-006-9239-z.

Hamilton, K., Y. O. Takahasi, and W. Ohfuchi, 2008: Mesoscale spectrum of atmospheric motions investigated in a very fine resolution global general circulation model. *J. Geophys. Res.*, **113**, D18110, doi:10.1029/2008JD009785.

Koshyk, J. N., and K. Hamilton, 2001: The horizontal kinetic energy spectrum and spectral budget simulated by a high-resolution troposphere–stratosphere–mesosphere GCM. *J. Atmos. Sci.*, **58**, 329–348, doi:10.1175/1520-0469(2001)058<0329:THKESA>2.0.CO;2.

——, B. A. Boville, K. Hamilton, E. Manzini, and K. Shibata, 1999: Kinetic energy spectrum of horizontal motions in middle-atmosphere models. *J. Geophys. Res.*, **104**, 27 177–27 190, doi:10.1029/1999JD900814.

Lilly, D. K., 1983: Stratified turbulence and the mesoscale variability of the atmosphere. *J. Atmos. Sci.*, **40**, 749–761, doi:10.1175/1520-0469(1983)040<0749:STATMV>2.0.CO;2.

Lindborg, E., 1999: Can the atmospheric kinetic energy spectrum be explained by two-dimensional turbulence? *J. Fluid Mech.*, **388**, 259–288, doi:10.1017/S0022112099004851.

——, 2006: The energy cascade in a strongly stratified fluid. *J. Fluid Mech.*, **550**, 207–242, doi:10.1017/S0022112005008128.

——, 2007: Horizontal wavenumber spectra of vertical vorticity and horizontal divergence in the upper troposphere and lower stratosphere. *J. Atmos. Sci.*, **64**, 1017–1025, doi:10.1175/JAS3864.1.

——, 2015: A Helmholtz decomposition of structure functions and spectra calculated from aircraft data. *J. Fluid Mech.*, **762**, R4, doi:10.1017/jfm.2014.685.

Marenco, A., and Coauthors, 1998: Measurement of ozone and water vapor by Airbus in-service aircraft: The MOZAIC airborne program, an overview. *J. Geophys. Res.*, **103**, 25 631–25 642, doi:10.1029/98JD00977.

Nastrom, G. D., and K. S. Gage, 1985: A climatology of atmospheric wavenumber spectra of wind and temperature observed by commercial aircraft. *J. Atmos. Sci.*, **42**, 950–960, doi:10.1175/1520-0469(1985)042<0950:ACOAWS>2.0.CO;2.

——, ——, and W. Jasperson, 1984: Kinetic energy spectrum of large- and mesoscale atmospheric processes. *Nature*, **310**, 36–38, doi:10.1038/310036a0.

Ricard, D., C. Lac, S. Riette, R. Legrand, and A. Mary, 2013: Kinetic energy spectra characteristics of two convection-permitting limited-area models AROME and Meso-NH. *Quart. J. Roy. Meteor. Soc.*, **139**, 1327–1341, doi:10.1002/qj.2025.

Selz, T., and G. C. Craig, 2015: Upscale error growth in a high-resolution simulation of a summertime weather event over Europe. *Mon. Wea. Rev.*, **143**, 813–827, doi:10.1175/MWR-D-14-00140.1.

Skamarock, W. C., 2004: Evaluating mesoscale NWP models using kinetic energy spectra. *Mon. Wea. Rev.*, **132**, 3019–3032, doi:10.1175/MWR2830.1.

——, J. B. Klemp, M. G. Duda, L. D. Fowler, S.-H. Park, and T. Ringler, 2012: A multiscale nonhydrostatic atmospheric model using centroidal Voronoi tesselations and C-grid staggering. *Mon. Wea. Rev.*, **140**, 3090–3105, doi:10.1175/MWR-D-11-00215.1.

——, S.-H. Park, J. B. Klemp, and C. Snyder, 2014: Atmospheric kinetic energy spectra from global high-resolution nonhydrostatic simulations. *J. Atmos. Sci.*, **71**, 4369–4381, doi:10.1175/JAS-D-14-0114.1.

VanZandt, T. E., 1982: A universal spectrum of buoyancy waves in the atmosphere. *Geophys. Res. Lett.*, **9**, 575–578, doi:10.1029/GL009i005p00575.

Vincent, R. A., and S. D. Eckermann, 1990: VHF radar observations of mesoscale motions in the atmosphere: Evidence for gravity wave Doppler shifting. *Radio Sci.*, **25**, 1019–1037, doi:10.1029/RS025i005p01019.

Waite, M. L., and C. Snyder, 2013: Mesoscale energy spectra of moist baroclinic waves. *J. Atmos. Sci.*, **70**, 1242–1256, doi:10.1175/JAS-D-11-0347.1.